

Chiral voltage propagation in a self-calibrated topoelectrical Chern circuit

Tobias Hofmann,^{1,*} Tobias Helbig,^{1,*} Ching Hua Lee,^{2,3} and Ronny Thomale^{1,†}

¹*Institute for Theoretical Physics and Astrophysics,
University of Würzburg, D-97074 Würzburg, Germany*

²*Department of Physics, National University of Singapore, Singapore, 117542.*

³*Institute of High Performance Computing, A*STAR, Singapore, 138632.*

(Dated: December 3, 2022)

Abstract

We propose an electric circuit array with topologically protected uni-directional voltage modes at its boundary. Instead of external bias fields or floquet engineering, we employ negative impedance converters with current inversion (INICs) to accomplish a non-reciprocal, time-reversal symmetry broken electronic network we call topoelectrical Chern circuit (TCC). The TCC features an admittance bulk gap fully tunable via the resistors used in the INICs, along with a stable chiral voltage boundary mode reminiscent of the Berry flux monopole present in the admittance band structure.

* Both authors equally contributed to this work.

† Corresponding author: rthomale@physik.uni-wuerzburg.de

Introduction. The Chern insulator is the mother state of topological band theory. Originally conceived by Haldane as a tight-binding model of electrons with broken time-reversal symmetry on a hexagonal lattice [1], its roots lie in the Berry phase experienced by the electrons in the lattice Brillouin zone as a compact parameter space of momentum [2, 3]. The lattice Chern number C is quantized to take integer values, as it counts the total charge of Berry flux monopoles. For a Chern insulator with open boundaries, this implies C chiral edge modes which experience topological protection against any kind of disorder and other imperfections, as there is no backscattering. Note that this induces a stronger protection than, for instance, topological insulators, where only elastic backscattering is prohibited by the symmetry-protected topological character.

As the Berry phase is a phenomenon of parameter space and does not rely on any property of the phase space of quantum electrons, the Chern insulator readily suggests itself for realization in manifold alternative degrees of freedom. Haldane and Raghu employed this insight to propose a Chern insulator in photonic crystals by use of the Faraday effect, where chiral edge modes would manifest as one-way waveguides [4]. This work inspired the subsequent formulation and realization of Chern bands in magneto-optical photonic crystals [5, 6], optical waveguides subject to a magnetic field [7] or floquet modulation [8], ultra-cold atomic gases [9], mechanical gyrotropic [10–12] and acoustic [13, 14] systems, as well as, most recently, coupled optical resonators [15] and exciton polariton metamaterials [16]. The nature and potential technological use of topological chiral edge modes crucially depends on the constituent degrees of freedom, the control over the bulk gap size, and the ability to prevent loss from affecting the edge signal. In all beforementioned physical systems, the latter is the most challenging aspect since, unless one intends to pump the Chern mode anyway, the edge signal exhibits significant decay despite its topological protection.

In this work, we propose a Chern insulator which is formed by the admittance band structure of an electric circuit array. Initially accomplished for the circuit analogue of a topological crystalline insulator [17–19], topoelectrical circuits [20, 21] have recently been found to host topological admittance band structures [22] of high complexity, including Weyl bands [20, 23, 24] as well as higher-order topological insulators [25, 26]. As we now move beyond the realm of RLC circuits, the combined time reversal symmetry and circuit reciprocity breaking through negative impedance converters with current inversion (INICs) [27] allow us to formulate a topoelectrical Chern circuit (TCC) without external bias fields or floquet engineering. We find topologically protected chiral voltage edge modes which, from the viewpoint of electrical engineering, bears resemblance to a voltage circulator. In contrast to previous Chern band realizations, our arrangement of active circuit elements allows for a recalibration of gain and loss to protect the topological chiral voltage signal from decay.

Topoelectrical Chern circuit. The TCC is formed by a periodically repeated circuit structure sketched in Fig. 1a. The circuit unit cell detailed in Fig. 1b consists of two nodes each of which is connected to three adjacent nodes through a capacitor C_0 and to six next-nearest neighbours through INICs, which are further characterized in Fig. 1c and [28]. The nodes are grounded by inductors L_0 as well as capacitors of capacitance $C_g \pm \Delta$ on alternating sub-lattices. Due to the graph nature of electrical circuits implicating a gauge degree of freedom of arranging the circuit components in real space, we need to choose a Bravais lattice vector gauge [22] for the TCC, which we fix as $\mathbf{a}_1 = (1, 0)$ and $\mathbf{a}_2 = (0, 1)$ amounting to a brick wall structure as shown in Fig. 1a. For an external AC frequency ω and two-dimensional reciprocal space implied by the brick wall gauge, the TCC circuit Laplacian [20] $J_{\text{TCC}}(\mathbf{k}; \omega)$ and the corresponding spectrum $j_{\text{TCC}}(\mathbf{k}; \omega)$ read

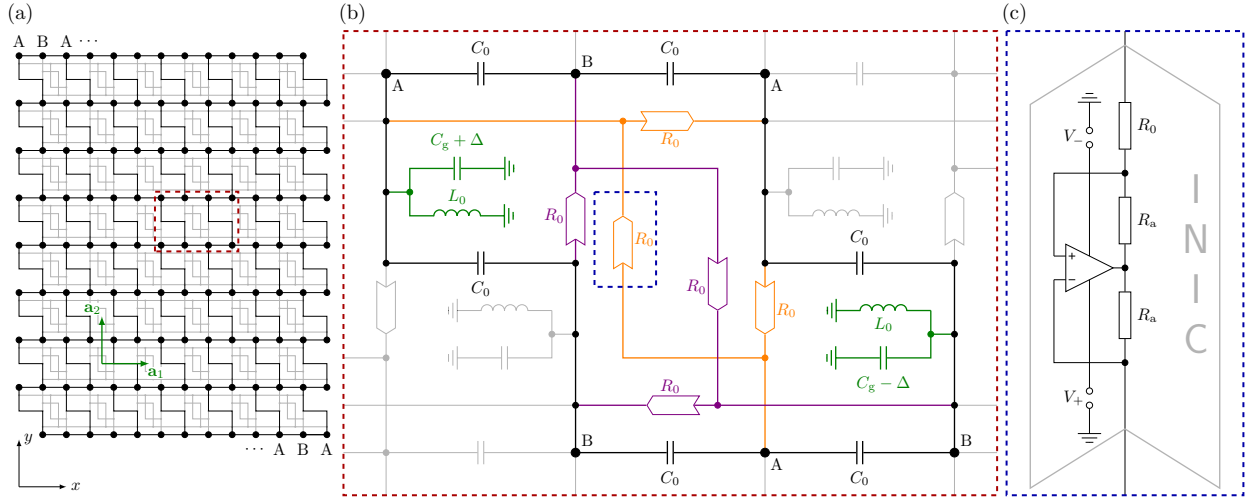


FIG. 1. Topoelectrical Chern circuit. (a) The three-coordinated circuit graph in a brick wall representation of horizontal (x) and vertical (y) alignment of nodes, where the circuit unit cell is given by two "sublattice" nodes A and B, and the Bravais vectors by \mathbf{a}_1 and \mathbf{a}_2 . (b) The detailed circuit element structure is illustrated for the red dashed framed rectangle in (a). Aside from capacitive inter-node connections C_0 , there exist inductive and capacitive connections to ground L_0 and $C_g \pm \Delta$, respectively. The other inter-node elements is the INIC highlighted by its resistive parameter R_0 . (c) The detailed INIC element structure is illustrated for the blue dashed framed rectangle in (b). The arrangement of resistors R_a and R_0 as well as an operational amplifier acts as a negative impedance converter configuration with current inversion [28].

$$J_{\text{TCC}}(\mathbf{k}; \omega) = i\omega \left[\left(3C_0 + C_g - \frac{1}{\omega^2 L_0} \right) \mathbb{1} - C_0 (1 + \cos(k_x) + \cos(k_y)) \sigma_x \right. \\ \left. - C_0 (\sin(k_x) + \sin(k_y)) \sigma_y + \left[\Delta + \frac{1}{\omega R_0} (\sin(k_x) - \sin(k_y) - \sin(k_x - k_y)) \right] \sigma_z \right] \quad (1)$$

and

$$j_{\text{TCC}}(\mathbf{k}; \omega) = i\omega \left[(3C_0 + C_g - \frac{1}{\omega^2 L_0}) \right. \\ \left. \pm \sqrt{C_0^2 (3 + 2 \cos(k_x) + 2 \cos(k_x - k_y) + 2 \cos(k_y)) + (\Delta + \frac{\Gamma(\mathbf{k})}{\omega})^2} \right], \quad (2)$$

where $\Gamma(\mathbf{k}) = \frac{1}{R_0} (\sin(k_x) - \sin(k_y) - \sin(k_x - k_y))$. In Fig. 2a, we show the projected band structure $j_{\text{TCC};x}(k_y)$ employing open-boundary condition in the x -direction obtained by an *LTS*pice simulation. It features the emergence of edge localized eigenstates, that reside inside the bulk band gap and as shown below propagate along the boundary of the TCC.

Emergence of chiral edge states due to the INIC configuration. The capacitive grounding parameter Δ effectively appears as an inversion symmetry breaking term reminiscent of a Semenoff mass. The topological character of the model roots in the INIC next-nearest neighbour hybridization elements, which break both time-reversal symmetry and circuit reciprocity via the effective implementation of a negative and positive resistance in the forward

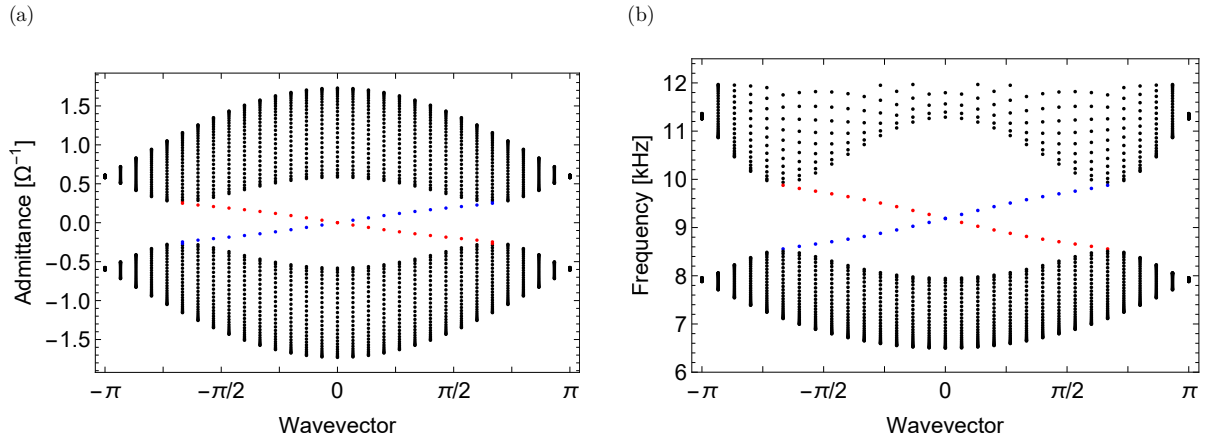


FIG. 2. TCC band structure. (a) Admittance band structure $j(\mathbf{k}, \omega)$ obtained from *LTS spice* simulations for open boundary conditions in x direction with an B – A-termination and periodic boundary conditions in y -direction. The chiral ingap edge modes are highlighted red and blue for the left and right termination, respectively. (b) Frequency band structure $\omega(\mathbf{k})$ obtained from numerical calculation for the same setting. TCC parameters are $C_0 = 10 \mu\text{F}$, $L_0 = 10 \mu\text{H}$, $R_0 = 20 \Omega$, $C_g = 0 \text{F}$, $\Delta = 0 \text{F}$ and $\omega = 2\pi 91.888 \text{ kHz}$. The system size is 30×30 unit cells. A chiral boundary admittance mode for the left and right x termination is seen in the bulk admittance as well as in the bulk frequency gap.

and reversed direction of the configuration respectively [28]. As seen in Fig. 1b, the linking of the INICs with either clockwise or counterclockwise orientation of their direction in a triangular shape effectively acts as a voltage circulator (VC), where a voltage profile on the three composite nodes can only travel in the direction indicated by the INIC [28]. During each timestep, the voltage profile applied to the VC is shifted by one node in the defined direction [28]. In the bulk of the TCC, after three timesteps, the voltage profile resumes its original distribution and has therefore traveled in a circular motion, effectively not propagating in any direction. The direction of this circular motion in the VC is of opposite sign for A and B sublattices generating a chiral symmetry breaking term proportional to σ_z . By this mechanism we induce an effective magnetic flux of $\phi = \frac{\pi}{2}$ adding up to zero in one plaquette and entering the phase of the next-nearest neighbor connection, whose magnitude is controlled by the resistance value. At the boundary of the TCC, the circular motion of the voltage profile is disrupted, because the VC needs to be disconnected at the edge unit cells to fulfill the open boundary conditions. The voltage profile bounces off the boundary generating a chiral voltage mode, which propagates along the edge of the TCC.

Symmetries. The incorporation of resistances in any circuit environment, such as implemented for the INIC in the TCC model breaks time-reversal symmetry (TRS) [28]. From the viewpoint of thermodynamics, this statement is trivial since any resistive component experiences Joule heating, converting electric potential energy to heat and leading to increased entropy and broken time-reversal symmetry. In terms of the Laplacian, TRS translates into $J = -J^*$ in real space and $J(\mathbf{k}) = -J^*(-\mathbf{k})$ in reciprocal space [28].

In the Laplacian formalism, circuit reciprocity is given by $J^\top = J$ in real space and by $J(\mathbf{k}) = J^\top(-\mathbf{k})$ in reciprocal space [28]. By the use of operational amplifiers [29] as active circuit elements, the INIC configuration acts as a charge source or sink to the system,

effectively producing an input or output current from ground to the system. This current feed from the INIC is arranged in such a way, that currents between two connected voltage nodes retain equal magnitude but flow in opposite directions, manifesting itself as a fully antisymmetric contribution to the grounded circuit Laplacian and thereby breaking reciprocity in terms of current inversion. We name our TCC hermitian iff its Laplacian matrix is anti-hermitian, i.e., $J = -J^\dagger$ which leads to purely imaginary admittance eigenvalues, and from there to real eigenfrequencies [28].

Hamiltonian formulation. The homogeneous equations of motion for an N -node circuit (no input currents, the circuit's time evolution is solely determined by its eigenfrequencies) can be re-written as $2N$ differential equations of first order as $-i \frac{d}{dt} \psi(t) = H \psi(t)$, where $\psi(t) := (\dot{\mathbf{V}}(t), \mathbf{V}(t))^\top$, i.e., the voltages and their first time derivatives are treated as independent variables. This defines the $2N \times 2N$ Hamiltonian block matrix H as the generator of the dynamic time evolution introduced in [28]. The time evolution of a given eigenstate $\psi_\alpha(t)$ yields $\psi_\alpha(t) = \psi_\alpha e^{i\omega_\alpha t}$ where the Hamiltonian's eigenvalues ω_α , $\alpha \in \{1, \dots, 2N\}$ are the resonance frequencies of the system (Fig. 2b), defined as the roots of the admittance eigenvalues $j(\omega_\alpha) = 0$ [28]. The projection of the bulk frequency spectrum to one direction with open boundary conditions, as depicted in Fig. 2b, is obtained by a numerical analysis. The emergence of a band gap in the admittance band structure is accompanied by an analogous gap opening in the frequency spectrum, leading to a correspondence of midgap resonances in Fig. 2b to midgap admittance eigenvalues in Fig. 2a.

Topological phase diagram. We define the Chern number for the lower admittance band

$$C = \frac{1}{2\pi} \oint_{BZ} d^2k \mathcal{B}(\mathbf{k}), \quad (3)$$

where $\mathcal{B}(\mathbf{k})$ denotes the Berry curvature [28]. Eq. 3 is invariant under a change of the Bravais lattice vector gauge, whose only consequence is a distortion of the Brillouin zone [22]. It gives

$$C = \frac{1}{2}(\text{sign} \left(\Delta + \frac{3\sqrt{3}}{2} \frac{1}{\omega R_0} \right) - \text{sign} \left(\Delta - \frac{3\sqrt{3}}{2} \frac{1}{\omega R_0} \right)), \quad (4)$$

which is nonzero if $\text{sign} \left(\Delta - \frac{3\sqrt{3}}{2} \frac{1}{\omega R_0} \right) < 0$. This integer number is established as the topological invariant of the TCC, because it is identical to the Chern number defined for the Hamiltonian governing the time evolution of the system. In the TCC regime, a propagation of chiral voltage boundary modes (Fig. 2) is present due to $\omega(\mathbf{k}) \neq \omega(-\mathbf{k})$ which is associated with the breaking of circuit reciprocity [28].

Simulation results. We aim to demonstrate the existence of propagating edge states as well as the variability and flexibility of the TCC, which enables us to customize the properties of the edge modes concerning foremost their propagation velocity, localization length and dispersion as well as dissipation effects by performing *LTSpice* simulations, whose results are shown in Fig. 3. The current excitation, which is fed into the circuit at one specified edge node is described by a Fourier transformed Gaussian distribution $\Delta\omega_G$ in frequency space centered around the frequency ω_c , which is chosen to be equal to the resonance frequency of the circuit ω_0 , where the imaginary admittance band structure is symmetric around $0 \Omega^{-1}$. It is furthermore characterized by a standard deviation of $\Delta\omega_{\text{exc}}$ selected to fully lie inside the frequency bulk band gap.

To be able to compare the admittance to the frequency bandgap, we define the relative admittance gap as the ratio of the minimal gap value at the K_\pm -point j_{gap} to the total

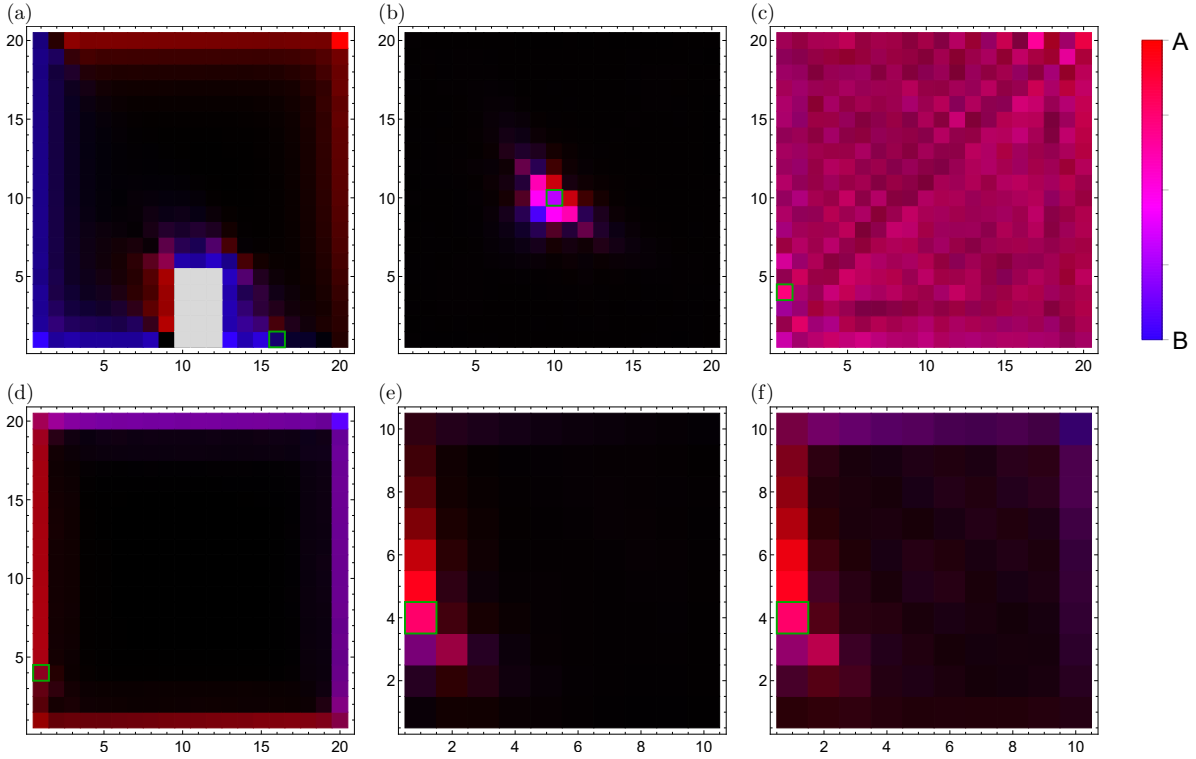


FIG. 3. Integrated voltage signal of a current excitation to the TCC in an *LTSpice* simulation plotted in a real space brick wall structure. The colour brightness corresponds to the amplitude of the added squared intensity at *A* and *B* sublattice at that unit cell. Excitation of the circuit by a Fourier transformed Gaussian wave packet, whose frequency range $\Delta\omega_G$ lies inside the bulk band gap. Excitation point marked by green framing. (a)-(d) 20×20 unit cells with *A*–*B*-termination, using ideal operational amplifiers and parasitic serial resistance of L_0 and C_0 of $R_{\text{ser},L_0} = 1 \text{ m}\Omega$, $R_{\text{ser},C_0} = 0 \text{ m}\Omega$, $\Delta = 0 \text{ F}$ and $C_g = 0 \text{ F}$. Circuit components chosen to $C_0 = 10 \mu\text{F}$, $L_0 = 10 \mu\text{H}$ and $R_0 = 10 \Omega$. (a) *B*–*A* termination. implementation of defect section of size 3×5 unit cells at the *x*-boundary. For (c) $\Delta\omega_G$ inside bulk band. (d) Implementation of random disorder with tolerances on capacitances $\delta C_0 = 2 \%$, inductances $\delta L_0 = 4 \%$ and resistances $\delta R_0 = 1 \%$. (e) and (f) 10×10 unit cells with *A*–*B*-termination, implementing realistic operational amplifiers (*LTSpice* model LT1363). Circuit components chosen to $C_0 = 0.1 \mu\text{F}$, $L_0 = 1 \mu\text{H}$ and $R_0 = 30 \Omega$. $R_{\text{ser},L_0} = 150 \text{ m}\Omega$, $R_{\text{ser},C_0} = 5 \text{ m}\Omega$, $\Delta = 0 \text{ F}$ and $C_g = 0 \text{ F}$. (f) Edge INIC connections to ground are adapted to be $R_0 = 36 \Omega$ for the positive and $R_0 = -16 \Omega$ for the negative component.

bandwidth at the Γ -point $j_{\text{BW}}(\omega)$

$$A_{\text{gap}} = \frac{j_{\text{BW}}}{j_{\text{gap}}} = \frac{\sqrt{3}}{2} \frac{1}{\omega R_0 C_0}. \quad (5)$$

The \mathbf{k} -spacing of the bearded ($\Delta\mathbf{k}_{\text{sp}} = \frac{4\pi}{3}$) to the zigzag edge ($\Delta\mathbf{k}_{\text{sp}} = \frac{2\pi}{3}$) attains a ratio of 2 : 1 due to their existence in different regimes of the projected Brillouin zone. We approximate a linear dispersion of the edge band inside the bulk gap $\omega_{\text{gap}} = \sqrt{3}/(2 R_0 C_0)$ in the frequency spectrum plotted in Fig. 2b and compute the group velocities of the zigzag

$(v_{G;zz})$ and bearded edge $(v_{G;zz})$ to

$$v_{G;zz} = \frac{\omega_{\text{gap}}}{\Delta k_{\text{sp}}} = \frac{3\sqrt{3}}{4\pi} \frac{1}{R_0 C_0} = 2 v_{G;\text{bd}}. \quad (6)$$

The group velocities have the same inverse proportionality to the parameters R_0 and C_0 as j_{gap} and therefore relate to it by a scaling via the frequency,

$$j_{\text{gap}} = \frac{2\pi}{3} \frac{v_{G,zz}}{\omega} = \frac{4\pi}{3} \frac{v_{G,\text{bd}}}{\omega}. \quad (7)$$

As seen in Fig. 3a, the edge mode is localized at the boundary and decays exponentially into the bulk of the TCC. The localization length of those edge modes is inversely proportional to the direct gap of the admittance spectrum at the corresponding \mathbf{k} -value and frequency ω . We can then estimate the upper bound of the localization length $\xi_{\text{loc};\text{min}}$ to occur at the Dirac cones, where the minimal gap is present and evaluate it to

$$\xi_{\text{loc};\text{min}} \approx \frac{2}{|j_{\text{gap}}|} = \frac{4R_0}{3\sqrt{3}} \quad (8)$$

at the resonance frequency ω_0 . As expected, the localization length is directly proportional to the resistance value in the INIC configuration, because this is the parameter regulating the gap size. The magnitude of excitation Π_n of the n^{th} eigenstate $\phi_n^\dagger(\omega)$ of the grounded circuit Laplacian J contains the same inverse proportionality to their eigenvalues written as

$$\Pi_n(\omega) = \frac{1}{j_n(\omega)} (\phi_n^\dagger(\omega) \mathbf{I}), \quad (9)$$

where \mathbf{I} is the vector of input currents exciting the Hermitian system. Consequently, all eigenstates that have a nonzero scalar product with the current excitation vector get excited to some amount, but are exponentially damped by the factor $\ln(j_n(\omega))$ depending on the distance of the corresponding eigenvalue to $0 \Omega^{-1}$ at that excitation frequency. In Fig. 3a, we show the Gaussian wave packet circulating in a counterclockwise motion along the boundary of the TCC, while experiencing a decrease in amplitude due to dissipation effects. It illustrates the strong localization of the propagating modes at the boundary. By consequence, if we either choose the point of excitation of the circuit in the bulk or $\Delta\omega_{\text{exc}}$ to lie inside the bulk admittance band, the order of excitation of the edge modes is decreased in relation to the excitation of bulk modes and the propagation along the edge is suppressed, which is demonstrated in Fig. 3b and 3c respectively, where no edge localization and propagation is present anymore. As observed in 3a, the amplitude of a propagating mode at the corner of the circuit is larger in relation to the neighbouring nodes, which roots in the fact, that the contribution due to the inner product $(\phi_n^\dagger(\omega) \mathbf{I})$ is the largest at that point.

To demonstrate the topological character of the edge modes, we implement a defect section at the boundary of the circuit shown in Fig. 3a, where the voltage nodes are being grounded directly and observe a propagation of the edge mode around this defect area. This proves the topological protection of the boundary mode, which solely roots in the existence of a nonzero Chern number and is not coupled to the boundary termination of the TCC. The same reasoning holds for an implementation of random distributed disorder to the components of the circuit shown in Fig. 3d. Due to the global topological protection of the edge states, it remains stable against local disorder of the components that does not exceed the order of magnitude of the admittance band gap.

By introducing parasitic effects in terms of effective serial resistances of the inductors and capacitors as well as using a realistic commercially available model for the OpAmp (*LTS* Spice

model LT1363), the wave packet dissipates during the propagation along the edge with an exponential decay that is an artifact of the shift of the real resonance frequencies to the positive imaginary axis as pictured in Fig. 3e.

Additionally to the dissipation, the Gaussian wave packet in the time domain experiences a dispersion broadening the time spread Δt_{wave} during the propagation, caused by the nonzero curvature of the frequency edge band close to the Dirac cone. Illustrating the tunability of the TCC, we can correct for the effect of dissipation due to parasitics by adjusting the INIC parameters connecting the edge nodes with ground accordingly and thereby increasing the decay length in a realistic system as shown in Fig. 3f.

Conclusion. We have introduced and analyzed the topoelectrical Chern circuit as a topological circuit array with active INIC elements. A topological voltage Chern mode not only appears due to the effect of the INICs on the admittance band structure, but, under fully realistic experimental conditions, also allows for a convenient calibration in terms of propagation properties and decay through the INIC. This reaches an unprecedented level at which a topological edge mode is tunable in all detail.

ACKNOWLEDGMENTS

We thank S. Imhof for helpful discussions. The work in Würzburg is supported by the European Research Council (ERC) through ERC-StG-Thomale-TOPOLECTRICS-336012 and by the German Research Foundation (DFG) through DFG-SFB 1170.

- [1] F. D. M. Haldane, Phys. Rev. Lett. **61**, 2015 (1988).
- [2] M. V. Berry, Proceedings of the Royal Society of London A: Mathematical, Physical and Engineering Sciences **392**, 45 (1984).
- [3] J. Zak, Phys. Rev. Lett. **62**, 2747 (1989).
- [4] F. D. M. Haldane and S. Raghu, Phys. Rev. Lett. **100**, 013904 (2008).
- [5] Z. Wang, Y. D. Chong, J. D. Joannopoulos, and M. Soljačić, Phys. Rev. Lett. **100**, 013905 (2008).
- [6] Z. Wang, Y. Chong, J. D. Joannopoulos, and M. Soljačić, Nature **461**, 772 (2009).
- [7] Z. Yu, G. Veronis, Z. Wang, and S. Fan, Phys. Rev. Lett. **100**, 023902 (2008).
- [8] M. C. Rechtsman, J. M. Zeuner, Y. Plotnik, Y. Lumer, D. Podolsky, F. Dreisow, S. Nolte, M. Segev, and A. Szameit, Nature **496**, 196 (2013).
- [9] G. Jotzu, M. Messer, R. Desbuquois, M. Lebrat, T. Uehlinger, D. Greif, and T. Esslinger, Nature **515**, 237 (2014).
- [10] C. L. Kane and T. C. Lubensky, Nature Physics **10**, 39 (2013).
- [11] L. M. Nash, D. Kleckner, A. Read, V. Vitelli, A. M. Turner, and W. T. M. Irvine, Proceedings of the National Academy of Sciences of the United States of America **112**, 14495 (2015).
- [12] P. Wang, L. Lu, and K. Bertoldi, Phys. Rev. Lett. **115**, 104302 (2015).
- [13] Z. Yang, F. Gao, X. Shi, X. Lin, Z. Gao, Y. Chong, and B. Zhang, Phys. Rev. Lett. **114**, 114301 (2015).
- [14] A. B. Khanikaev, R. Fleury, S. H. Mousavi, and A. Alù, Nature Communications **6**, 8260 (2015).

- [15] M. A. Bandres, S. Wittek, G. Harari, M. Parto, J. Ren, M. Segev, D. N. Christodoulides, and M. Khajavikhan, *Science* (2018).
- [16] S. Klembt, T. H. Harder, O. A. Egorov, K. Winkler, R. Ge, M. A. Bandres, M. Emmerling, L. Worschech, T. C. H. Liew, M. Segev, C. Schneider, and S. Höfling, arXiv:1808.03179.
- [17] L. Fu, *Phys. Rev. Lett.* **106**, 106802 (2011).
- [18] J. Ningyuan, C. Owens, A. Sommer, D. Schuster, and J. Simon, *Phys. Rev. X* **5**, 021031 (2015).
- [19] V. V. Albert, L. I. Glazman, and L. Jiang, *Phys. Rev. Lett.* **114**, 173902 (2015).
- [20] C. H. Lee, S. Imhof, C. Berger, F. Bayer, J. Brehm, L. W. Molenkamp, T. Kiessling, and R. Thomale, *Communications Physics* **1**, 39 (2018).
- [21] L. Lu, *Nature Physics* **14**, 875 (2018).
- [22] T. Helbig, T. Hofmann, C. H. Lee, R. Thomale, S. Imhof, L. W. Molenkamp, and T. Kiessling, arXiv:1807.09555.
- [23] K. Luo, R. Yu, and H. Weng, *Research* **2018**, 6793752 (2018).
- [24] Y. Lu, N. Jia, L. Su, C. Owens, G. Juzliunas, D. I. Schuster, and J. Simon, arXiv:1807.05243.
- [25] S. Imhof, C. Berger, F. Bayer, J. Brehm, L. W. Molenkamp, T. Kiessling, F. Schindler, C. H. Lee, M. Greiter, T. Neupert, and R. Thomale, *Nature Physics* **14**, 925 (2018).
- [26] M. Serra-Garcia, R. Süsstrunk, and S. D. Huber, arXiv:1806.07367.
- [27] W.-K. Chen, *The Circuits and Filters Handbook*, 3rd ed. (CRC Press, Inc., Boca Raton, FL, USA, 2009).
- [28] see Supplementary Information.
- [29] Z. Wang, Z. Wang, J. Wang, B. Zhang, J. Huangfu, J. D. Joannopoulos, M. Soljačić, and L. Ran, *Proceedings of the National Academy of Sciences* **109**, 13194 (2012).

Appendix A: Negative impedance converter (INIC)

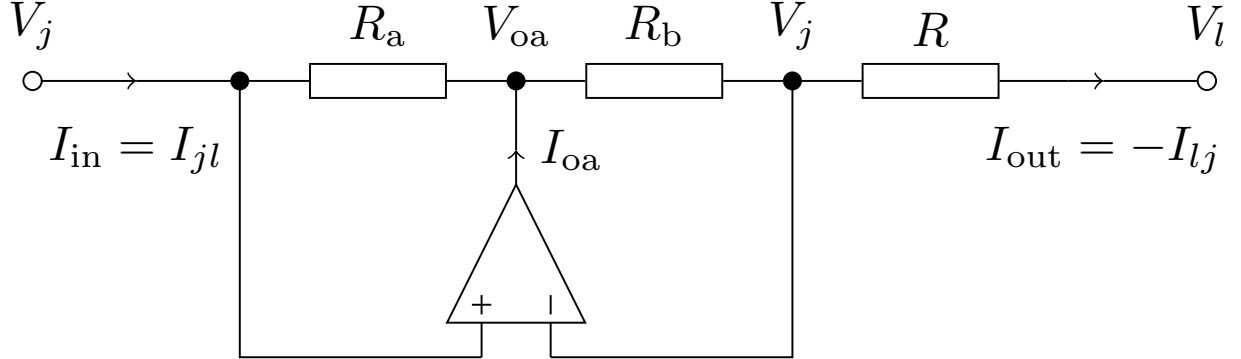


FIG. 4. Circuit diagram of an operational amplifier in a negative impedance converter configuration with current inversion.

For the realization of a negative impedance converter [27] we use an operational amplifier (OpAmp) in the configuration shown in Fig. 4. In the following we will derive its Laplacian matrix $J_{\text{NIC}} = \Sigma_{\text{NIC}}$. The current entering the INIC from the left is given by $I_{\text{in}} = (V_j - V_{\text{oa}})/R_a$ and the current leaving on the right by $I_{\text{out}} = (V_j - V_l)/R$ as the OpAmp is operated in a negative feedback configuration. Since the inputs of the OpAmp are assumed to have infinite impedance, no current is flowing into them, and I_{out} is also given by $I_{\text{out}} = (V_{\text{oa}} - V_l)/R_b$. Solving these equations for I_{in} yields

$$I_{\text{in}} = -\frac{R_b}{R_a \cdot R} (V_j - V_l), \quad (10a)$$

$$I_{\text{out}} = \frac{1}{R} (V_j - V_l). \quad (10b)$$

Translating these results in Laplacian language features the node voltage equation

$$\begin{pmatrix} I_{jl} \\ I_{lj} \end{pmatrix} = \frac{1}{R} \begin{pmatrix} -\nu & \nu \\ -1 & 1 \end{pmatrix} \begin{pmatrix} V_j \\ V_l \end{pmatrix}, \quad (11)$$

where $\nu = R_a/R_b$. The matrix is not symmetric and circuit reciprocity is therefore broken. To obtain an anti-Hermitian Laplacian as desired in the TCC, we require $\nu = 1$, *i.e.* $R_a = R_b$. If this is not the case, the eigenfrequencies of the system get complex resulting either in a damping or an instability. In the analysis of the TCC, the INICs are trimmed to the edge of stability. In a real experiment it needs to be ensured that the system operates stable, accepting overall loss. Parasitic effects may help to turn the circuit towards the stable regime. However, since electric circuits are easily tunable, *e.g.* resistors can be implemented by individually adjustable potentiometers, the interplay between robust stability and low dissipation can be fine-tuned to the desired sweet spot.

Appendix B: Hamiltonian formulation

We define voltage and current vectors by denoting the voltages measured at the nodes of a circuit board against ground, and the input currents at the nodes by N -component vectors

\mathbf{V} and \mathbf{I} , respectively. The equations of motion a circuit are given by

$$\frac{d}{dt}\mathbf{I}(t) = C \frac{d^2}{dt^2}\mathbf{V}(t) + \Sigma \frac{d}{dt}\mathbf{V}(t) + L \mathbf{V}(t), \quad (12)$$

where capacitance C , conductance Σ , and inductance L are the real-valued $(N \times N)$ -matrices forming the grounded circuit Laplacian [20] by

$$J(\omega) = i\omega C + \Sigma + \frac{1}{i\omega} L. \quad (13)$$

The homogeneous equations of motion ($\mathbf{I} = 0$, where the circuit's time evolution is solely determined by its eigenfrequencies) can be re-written as $2N$ differential equations of first order as

$$-i \frac{d}{dt} \psi(t) = H \psi(t), \quad (14)$$

where $\psi(t) := (\dot{\mathbf{V}}(t), \mathbf{V}(t))^\top$, i.e., the voltages and their first time derivatives are treated as independent variables.

This defines the $2N \times 2N$ Hamiltonian block matrix

$$H_{\text{TCC}} = i \begin{pmatrix} C^{-1}\Sigma & C^{-1}L \\ -\mathbb{1} & 0 \end{pmatrix} \quad (15)$$

where, for the TCC in reciprocal space as in Eq. 1,

$$\begin{aligned} C(\mathbf{k}) &= (3C_0 + C_g) \mathbb{1} + C_0 (1 + \cos(k_x) + \cos(k_y)) \sigma_x \\ &\quad + C_0 (\sin(k_x) + \sin(k_y)) \sigma_y + \Delta \sigma_z, \end{aligned} \quad (16a)$$

$$\Sigma(\mathbf{k}) = \frac{i}{R_0} (\sin(k_x) - \sin(k_y) - \sin(k_x - k_y)) \sigma_z, \quad (16b)$$

$$L(\mathbf{k}) = \frac{1}{L_0} \mathbb{1}. \quad (16c)$$

The time evolution of a given eigenstate $\psi_\alpha(t)$ yields $\psi_\alpha(t) = \psi_\alpha e^{i\omega_\alpha t}$ where the eigenvalues ω_α , $\alpha \in \{1, \dots, 2N\}$ are the resonance frequencies of the system (Fig. 2), defined as the roots of the admittance eigenvalues $j(\omega_\alpha) = 0$ [28]. To render the measurable voltage \mathbf{V} and its time derivative $\dot{\mathbf{V}}$ real, the eigenfrequencies of the Hamiltonian must occur in pairs of $(\omega_\alpha, -\omega_\alpha^*)$ corresponding to complex conjugated pairs of eigenstates $\psi_\alpha, \psi_\alpha^*$. This enables us to label the eigenvalues by ω_n^\pm with $n = 1, \dots, N$. In Bloch form we label the eigenfrequencies by their corresponding wavenumber \mathbf{k} and band index m as $n = (\mathbf{k}, m)$. This frequency-wave number mapping of the eigenvalues of the Hamiltonian defines the frequency spectrum $\omega(\mathbf{k})$ in reciprocal space. Due to the linking of the spectra, the emergence of a band gap in the admittance band structure is accompanied by an analogous gap opening in the frequency spectrum. The eigenvectors of the Hamiltonian can be constructed out of the eigenvectors of the Laplacian according to

$$\psi_n^+ = \begin{pmatrix} i\omega_n \mathbf{V}_n \\ \mathbf{V}_n \end{pmatrix} \quad \text{and} \quad \psi_n^- = \begin{pmatrix} -i\omega_n^* \mathbf{V}_n^* \\ \mathbf{V}_n^* \end{pmatrix}. \quad (17)$$

These are right eigenvectors. Note that the left eigenvectors of the non-Hermitian Hamiltonian may differ.

Appendix C: Detailed symmetry analysis

Written in the form of equation (13), it becomes clear, that the Laplacian is Hermitian, if C and L are Hermitian matrices, while Σ must be anti-Hermitian, which is fulfilled for the TCC Laplacian.

Time reversal is defined as the operation of taking $t \rightarrow -t$. As a consequence, voltages transform even and currents odd under time reversal. Concluding from the time-reversed form of equation (12), we call a circuit to be time reversal symmetric (TRS) if $\Sigma = 0$, which is equivalent to excluding any resistive component in the circuit, where energy can dissipate. This condition can be reformulated as allowing only for fully imaginary real space Laplacians and is in accordance to the TRS condition $J^* = -J$ in real space defined in the main text, which can be checked by insertion into (13). Translated into reciprocal space, the TRS condition yields $J^*(\mathbf{k}) = -J(-\mathbf{k})$.

As a visualization of circuit reciprocity, consider two voltage nodes of the circuit with labels j and l connected by a passive circuit element. The current flowing out of node j must be the current entering at node l . In other words, the current running from j to l , I_{jl} , is the negative of the current running from l to j , *i.e.* $I_{jl} = -I_{lj}$. This behaviour is called circuit reciprocity. In the Laplacian formalism, circuit reciprocity is given by $J_{jl} = J_{lj}$ or $J^\top = J$ in real space and by $J(\mathbf{k}) = J^\top(-\mathbf{k})$ in Bloch form. In the present implementation, we use operational amplifiers as active circuit elements in an INIC configuration to tune the system to the point where $I_{jl} = I_{lj}$ for the INIC connection. Other implementations of broken circuit reciprocity use magnetic fields or sophisticated transistor arrays such as in passive circulators developed for electrical communication engineering. On the grounds, that the resonance frequencies for $j(\omega, \mathbf{k}) = 0$ are identical to the eigenvalues of the Hamiltonian, we obtain the symmetry

$$\omega(\mathbf{k}) = \omega(-\mathbf{k}) \quad (18)$$

for the frequency spectrum. The voltage eigenmodes of a periodic system are constructed out of Bloch waves in reciprocal space and retrieve the form of plane waves labeled by the wave number \mathbf{k} ,

$$\mathbf{V}_{\mathbf{k},n}(\mathbf{r}, t) = \mathbf{V}_{\mathbf{k},n} e^{i\mathbf{k} \cdot \mathbf{r}} e^{i\omega_n(\mathbf{k})t}. \quad (19)$$

For the following considerations, we assume a Hermitian circuit system. If it is additionally time-reversal symmetric and reciprocal, the eigenmodes for inverse \mathbf{k} are characterized by

$$\mathbf{V}_{-\mathbf{k},n}(\mathbf{r}, t) = \mathbf{V}_{\mathbf{k},n} e^{-i\mathbf{k} \cdot \mathbf{r}} e^{i\omega_n(\mathbf{k})t}. \quad (20)$$

by using $\mathbf{V}_{-\mathbf{k},n} = \mathbf{V}_{\mathbf{k},n}$ and $\omega(-\mathbf{k}) = \omega(\mathbf{k})$. Those eigenmodes for negative \mathbf{k} travel in the opposite direction than those corresponding to \mathbf{k} and ultimately combine to standing waves, that experience no propagation in any direction in a steady-state solution of the system. A propagation can only be induced by breaking the symmetry $\omega(-\mathbf{k}) = \omega(\mathbf{k})$, which is solely possible by a breaking of time reversal symmetry and reciprocity. Consequently, it is not possible to obtain propagating modes in such a reciprocal system. As detailed in the main text, the INIC configuration implementing for the next-nearest neighbor hopping elements breaks time reversal symmetry and reciprocity simultaneously, inducing unidirectional propagation in one direction along the boundary of the TCC in the topological regime. This roots in the fact, that the frequency midgap eigenstates in an open-boundary termination in one direction introduce the asymmetry $\omega(\mathbf{k}) \neq \omega(-\mathbf{k})$.

The states associated with the midgap admittance and frequency bands in Fig. 2a and 2b of the main text linking the two Dirac cones are inherently localized at opposing edges of the circuit due to the breaking of chiral symmetry

$$\mathcal{C} : \sigma_z J \sigma_z = -J \quad (21)$$

by the mass term $i(\omega\Delta + \Gamma(\mathbf{k}))\sigma_z$ defined in the main text. In this way, the eigenmodes attain a chiral character and it becomes possible to initiate a voltage wave packet at the boundary of the TCC, which travels along the edge of the circuit in one direction.

Appendix D: Hermitian circuit

In the following, we show, that the resonance frequencies as eigenvalues of the Hamiltonian are real-valued, if we are dealing with a Hermitian system and therefore experience no dissipation.

Lemma. Let a circuit network consisting of N nodes be described by a circuit Laplacian J in real space, which can be divided into contributions of different circuit elements according to equation (13). Moreover, let all capacitances and inductances in the Laplacian be positive. If the Laplacian matrix is anti-Hermitian, $J = -J^\dagger$ for all real frequencies ω , then the eigenfrequencies of the corresponding Hamiltonian (15) are real.

Proof. If $J = -J^\dagger$, $\forall \omega \in \mathbb{R}$, it means that $C = C^\dagger$, $L = L^\dagger$ and $i\Sigma = (i\Sigma)^\dagger$. Consider the quadratic forms

$$c(\mathbf{V}) = \mathbf{V}^\dagger C \mathbf{V}, \quad (22a)$$

$$\sigma(\mathbf{V}) = \mathbf{V}^\dagger i\Sigma \mathbf{V}, \quad (22b)$$

$$l(\mathbf{V}) = \mathbf{V}^\dagger L \mathbf{V}, \quad (22c)$$

which are real for all complex N -vectors \mathbf{V} , since the representing matrices are Hermitian. Because of the structure of the Laplacian matrices and the assumption of not considering negative capacitances or inductances, L and C are weakly diagonally dominant matrices. Moreover, all entries of the matrices are real as we consider a Laplacian in real space and the elements on the diagonal are non-negative. Therefore, the matrices are positive semi-definite and $c(\mathbf{V}), l(\mathbf{V}) \geq 0$, $\forall \mathbf{V} \in \mathbb{C}^N$.

Now assume that $\psi_n = (i\omega_n V_n, V_n)^\top$ is an eigenvector of the Hamiltonian to eigenvalue ω_n . Then the equation

$$i\omega_n c(\mathbf{V}_n) - i\sigma(\mathbf{V}_n) + \frac{1}{i\omega_n} l(\mathbf{V}_n) = 0 \quad (23)$$

must hold. For $\omega_n \neq 0$ and $c(\mathbf{V}_n) \neq 0$ (trivial cases) we can solve the quadratic equation for the eigenfrequency by completing the square. We obtain

$$\omega_n = \frac{1}{c(\mathbf{V}_n)} \left(\sigma(\mathbf{V}_n) \pm \sqrt{\sigma^2(\mathbf{V}_n) + 4c(\mathbf{V}_n)l(\mathbf{V}_n)} \right) \quad (24)$$

which is real, because $c(\mathbf{V}_n)$ and $l(\mathbf{V}_n)$ are nonnegative real numbers. \square

Appendix E: Berry phase in Hamiltonian and Laplacian formulation

The Chern number is originally defined for the Hamiltonian as it is the generator of time translation and therefore determines the time evolution of the system. In the following, we show that for a time-independent, Hermitian system, $J = -J^\dagger$, the Berry phase and the Chern number, which are usually defined using the Hamiltonian eigenvectors, can be equally computed using the Laplacian eigenvectors. Consider the Berry connection $\mathcal{A}_n(\mathbf{k})$ defined as

$$\mathcal{A}_m(\mathbf{k}) = i \psi_m^\dagger(\mathbf{k}) \partial_{\mathbf{k}} \psi_m(\mathbf{k}). \quad (25)$$

Here ψ_m are the right eigenvectors of the Hamiltonian. Although the system is Hermitian in the sense defined in the main text, that the Laplacian is anti-Hermitian and the eigenfrequencies are real, the left eigenvectors may differ from the right eigenvectors. The latter can be expressed using the eigenvectors \mathbf{V}_m of the Laplacian,

$$\psi_m(\mathbf{k}) = \frac{1}{N_m(\mathbf{k})} \begin{pmatrix} i\omega_m(\mathbf{k}) \mathbf{V}_m(\mathbf{k}) \\ \mathbf{V}_m(\mathbf{k}) \end{pmatrix}, \quad (26)$$

where the $V_m(\mathbf{k})$ are assumed to be normalized, such that $N_m(\mathbf{k}) = \sqrt{\omega_m^2(\mathbf{k}) + 1}$ is the normalization of the Hamiltonian eigenvectors. Computing the derivative of an eigenvector while omitting the band indices yields

$$\partial_{\mathbf{k}} \psi = \frac{1}{N} \left[\begin{pmatrix} i(\partial_{\mathbf{k}} \omega) \mathbf{V} \\ 0 \end{pmatrix} + \begin{pmatrix} i\omega \partial_{\mathbf{k}} \mathbf{V} \\ \partial_{\mathbf{k}} \mathbf{V} \end{pmatrix} - \psi \partial_{\mathbf{k}} N \right]. \quad (27)$$

The projection of this result on ψ^\dagger exploiting the normalization of the Laplacian eigenvectors reads

$$\psi^\dagger \partial_{\mathbf{k}} \psi = \frac{1}{N^2} [\omega_n \partial_{\mathbf{k}} \omega + N^2 \mathbf{V}^\dagger \partial_{\mathbf{k}} \mathbf{V} - N \partial_{\mathbf{k}} N]. \quad (28)$$

Since $N \partial_{\mathbf{k}} N = \omega (\partial_{\mathbf{k}} \omega)$, the first and last term in the bracket cancel and we eventually find

$$\mathcal{A}_m(\mathbf{k}) = i \mathbf{V}_m^\dagger(\mathbf{k}) \partial_{\mathbf{k}} \mathbf{V}_m(\mathbf{k}). \quad (29)$$

That means that the Berry connection and therefore Berry curvature and Chern number for the (right) Hamiltonian and Laplacian eigenvectors coincide. Note, that the left eigenvectors or right and left eigenvectors of H combined may give alternative Berry connections and curvatures. However, the associated Chern numbers are equal. [?] In this regard the admittance and frequency band structure of a Hermitian system is topologically equivalent.

Appendix F: Topological circuit invariant

The TCC Laplacian in its two-band Bloch form in (1) of the main text can be recast in terms of the Pauli matrices σ_x , σ_y and σ_z as $J_{\text{TCC}}(k_x, k_y) = i (d_0 + \vec{d}(\mathbf{k}) \cdot \vec{\sigma})$ with

$$d_0 = \omega \left(3C_0 + C_g - \frac{1}{\omega^2 L_0} \right) \quad (30a)$$

$$d_x = -\omega C_0 (1 + \cos(k_x) + \cos(k_y)) \quad (30b)$$

$$d_y = -\omega C_0 (\sin(k_x) + \sin(k_y)) \quad (30c)$$

$$d_z = \omega \Delta + \frac{1}{R_0} (\sin(k_x) - \sin(k_y) - \sin(k_x - k_y)) \quad (30d)$$

It features an inversion symmetry breaking Semenoff mass $i\omega\Delta$ and a reciprocity and time reversal symmetry breaking Haldane mass $i\Gamma(\mathbf{k};\omega)$, which both open a band gap due to their appearance in $d_z(\mathbf{k})$. We can compute the effective low admittance theory at the Dirac cones at $\mathbf{K}_+ = (2\pi/3, 4\pi/3)$ and $\mathbf{K}_- = (4\pi/3, 2\pi/3)$ by expanding $\mathbf{k} = \mathbf{K}_\pm + \mathbf{q}$ up to first order in \mathbf{q} as

$$\begin{aligned} J_{\text{TCC,eff}}^{(\pm)}(\mathbf{q}) = & i\omega \left[\left(3C_0 + C_g - \frac{1}{\omega^2 L_0} \right) \mathbb{1} \right. \\ & \mp C_0 \frac{\sqrt{3}}{2} (q_y - q_x) \sigma_x + C_0 \frac{1}{2} (q_x + q_y) \sigma_y \\ & \left. + \left(\Delta \pm \frac{1}{\omega R_0} \frac{3\sqrt{3}}{2} \right) \sigma_z \right] + \mathcal{O}(\mathbf{q}^2), \end{aligned}$$

where the \pm -signs represent the positive and negative chirality of the Dirac cones with admittance gapping mass terms of $m_\pm = \Delta \pm \frac{1}{\omega R_0} \frac{3\sqrt{3}}{2}$ respectively. We can implement a linear transformation in (q_x, q_y) by

$$\frac{\sqrt{3}}{2} (q_y - q_x) \rightarrow p_y, \quad (31)$$

$$\frac{1}{2} (q_x + q_y) \rightarrow p_x, \quad (32)$$

which manifests as a distortion of the Brillouin zone, that doesn't affect the physics, but instead implements a different choice of Bravais lattice vector gauge than the one chosen in the main text. Neglecting the term proportional to the unit matrix gives the transformed low admittance TCC Laplacian

$$\frac{1}{i\omega} J_{\text{TCC,eff}}^{(\pm)}(\mathbf{p}) = \mp C_0 p_y \sigma_x + C_0 p_x \sigma_y + \left(\Delta \pm \frac{1}{\omega R_0} \frac{3\sqrt{3}}{2} \right) \sigma_z + \mathcal{O}(\mathbf{p}^2). \quad (33)$$

The sign of the Haldane mass $\Gamma(\mathbf{K}_\pm) = \pm \frac{1}{\omega R_0} \frac{3\sqrt{3}}{2}$ is correlated with the chirality of the Dirac cones, effectively yielding mass terms with opposing signs at the Dirac cones, while the Semenoff mass stays invariant throughout the whole BZ. The Haldane mass therefore induces a Berry flux monopole at both Dirac cones with half integer Berry charge each rendering a nonzero Chern number, but with opposite sign. The mapping $T^2 \rightarrow S^2 : (k_x, k_y) \mapsto \hat{\mathbf{d}} = \vec{d}/|d|$ from the torus to the unit sphere establishes the Chern number as the winding number of the vector $\hat{\mathbf{d}}$ as a covering of the unit sphere. In the TCC model, this winding number is $1/2$ for each Dirac cone due to the half covering of the unit sphere by the mappings of $\hat{\mathbf{d}}$ for each cone. The Chern number of the admittance band structure as defined in a gauge-invariant scheme in the main text by equation (3) resorts to the introduction of the Berry curvature. The Berry curvature of the lower band of the two-band model is given by

$$\mathcal{B}(\mathbf{k}) = \frac{1}{2} \hat{\mathbf{d}} \left(\frac{\partial \hat{\mathbf{d}}}{\partial k_x} \times \frac{\partial \hat{\mathbf{d}}}{\partial k_y} \right). \quad (34)$$

We want to show now, that in a reciprocal or time reversal symmetric system, the Chern number vanishes due to the antisymmetry of the Berry curvature in reciprocal space. While assuming a system, which preserves reciprocity, the circuit Laplacian has to fulfill the condition $J^\top(-\mathbf{k}) = J(\mathbf{k})$. This leads to individual constraints on the components of the

d-vector

$$d_0(-\mathbf{k}) = d_0(\mathbf{k}), \quad (35a)$$

$$d_x(-\mathbf{k}) = d_x(\mathbf{k}), \quad (35b)$$

$$d_y(-\mathbf{k}) = -d_y(\mathbf{k}), \quad (35c)$$

$$d_z(-\mathbf{k}) = d_z(\mathbf{k}). \quad (35d)$$

We can then use these conditions to compute the Berry curvature (34) of a reciprocal system for inverse wave vectors

$$\begin{aligned} \mathcal{B}(-\mathbf{k}) &= \frac{1}{2} \hat{\mathbf{d}}(-\mathbf{k}) \left(\frac{\partial \hat{\mathbf{d}}(-\mathbf{k})}{\partial k_x} \times \frac{\partial \hat{\mathbf{d}}(-\mathbf{k})}{\partial k_y} \right) \\ &= -\mathcal{B}(\mathbf{k}) \end{aligned} \quad (36)$$

by insertion of equations (35b) - (35d). In a time-reversal symmetric system exploiting the condition $-J^*(-\mathbf{k}) = J(\mathbf{k})$, there follows

$$d_0^*(-\mathbf{k}) = d_0(\mathbf{k}), \quad (37a)$$

$$d_x^*(-\mathbf{k}) = d_x(\mathbf{k}), \quad (37b)$$

$$d_y^*(-\mathbf{k}) = -d_y(\mathbf{k}), \quad (37c)$$

$$d_z^*(-\mathbf{k}) = d_z(\mathbf{k}). \quad (37d)$$

For Hermitian systems, the conditions (37b) -(37d) equal those for reciprocal systems, because the **d**-vector must be real. In such a case, equation (36) is also trivially fulfilled. The TCC model is a Hermitian model by construction, which means, that while omitting the next-nearest neighbor hopping terms, the Chern number must be zero, because it consists of an integration over the Berry curvature, which is an odd function in \mathbf{k} . Only by breaking time-reversal symmetry and reciprocity through the INIC next-nearest neighbor connection can the Chern number be nonzero. This establishes the combined breaking of reciprocity and time reversal symmetry in a circuit context as the direct analogue of time reversal symmetry breaking in a quantum system.

In Appendix D, we show, that the Berry phase and consequently the Chern number is identical in the Hamiltonian and Laplacian formalisms. We can therefore establish the admittance band Chern number as a topological invariant of the circuit dynamics. In our TCC model, we set the phase originating from the magnetic flux in the next-nearest neighbor hopping term to $\phi = \frac{\pi}{2}$, but in full generality an arbitrary phase ϕ is possible by incorporating the desired complex impedance in the INIC configuration. However, $\pi/2$ is the favoured configuration as it features the largest bandgap. By terminating the circuit in an arbitrary direction, we expect to acquire edge modes, that are exponentially localized at the boundary between a topologically nontrivial and trivial regime.

The Chern number for the lower band of the TCC model amounts to the combination of the Chern numbers caused by the half-charged Berry flux monopoles at each Dirac cone

$$\begin{aligned} C &= \frac{1}{2} (\text{sign}(m_+) - \text{sign}(m_-)) \\ &= \frac{1}{2} \left(\text{sign} \left(\Delta + \frac{3\sqrt{3}}{2} \frac{1}{\omega R_0} \right) - \text{sign} \left(\Delta - \frac{3\sqrt{3}}{2} \frac{1}{\omega R_0} \right) \right), \end{aligned}$$

which is nonzero if $\text{sign} \left(\Delta - \frac{3\sqrt{3}}{2} \frac{1}{\omega R_0} \right) < 0$ in agreement to the main text. In Fig. 5, we show the phase diagram of the TCC model as a function of the capacitive ground term Δ and

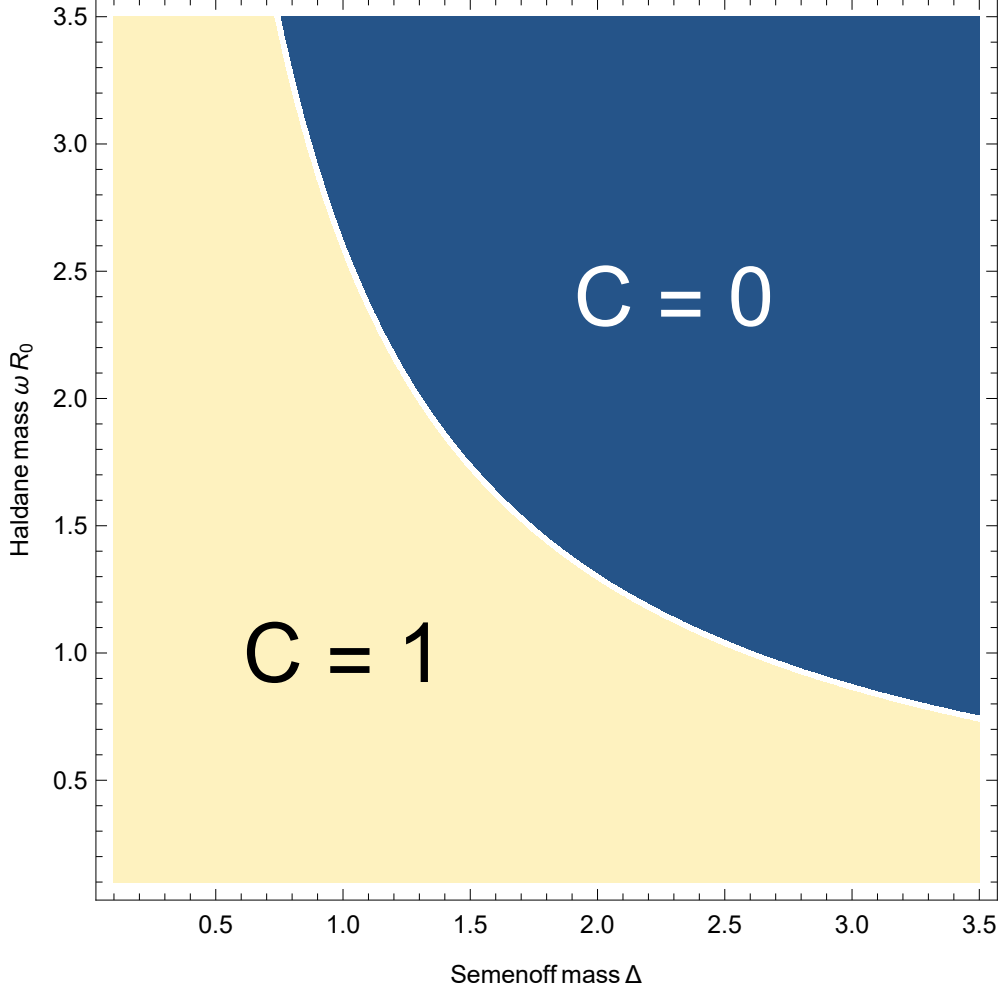


FIG. 5. Topological Phase Diagram of the TCC model as a function of the capacitive grounding term Δ and the combination of frequency and INIC resistance ωR_0 , both restricted to positive values only. The topological regime is marked by the Chern number $C = 1$ (yellow), whereas the topologically trivial phase has vanishing Chern number $C = 0$ (blue).

the combination of frequency and INIC resistance ωR_0 , which we both restrict to positive values only. The topological regime is marked by the Chern number $C = 1$, whereas the topologically trivial phase has vanishing Chern number. As expected, in the limit of $\Delta \rightarrow 0$, we are always in the topological regime, no matter how we choose ωR_0 . For larger Δ , the parameter ωR_0 needs to be reduced in an inversely proportional fashion to Δ in order to stay in the topological regime. The line of phase transition is determined by the condition

$$\omega R_0 = \frac{3\sqrt{3}}{2\Delta}. \quad (38)$$

Appendix G: Further simulations on the TCC edge mode dynamics

At a spatial transition between the topological to the trivial phase (as defined in Fig. 5) of a TCC, we expect a boundary mode exponentially localized at the introduced domain wall. As explained in the main text, the circuit is excited at one voltage node by a wave

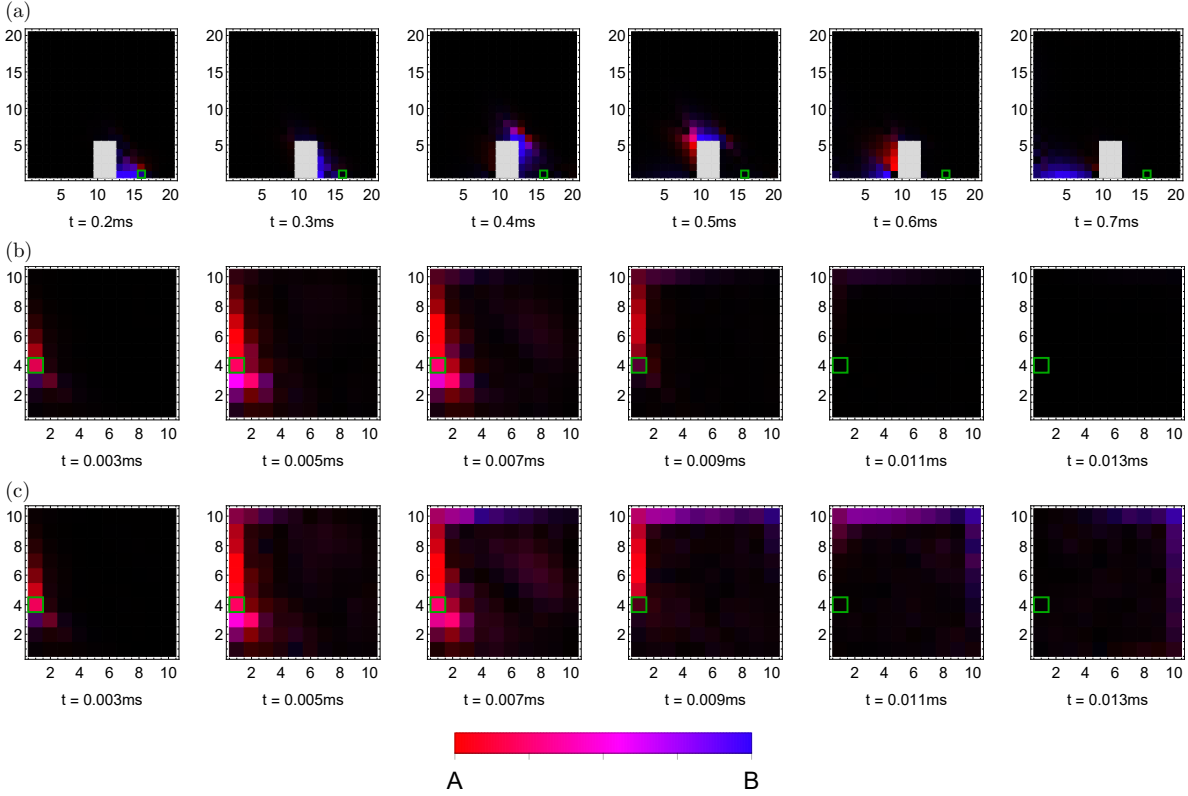


FIG. 6. Site resolved voltage signal of a current excitation applied to the TCC in an *LTSpice* simulation for different timesteps plotted in a real space brick wall structure. The colour coding corresponds to full support on the *A* (red) or *B* (blue) sublattice and interpolations thereof. The colour brightness corresponds to the amplitude of the added squared intensity of *A* and *B* sublattice at that unit cell. Excitation of the circuit by a Gaussian wave packet lying inside the bulk frequency band gap of the TCC. (a) 20×20 unit cells with *B* – *A*-termination in *x*- and *y*-direction, implementing ideal operational amplifiers, $R_{\text{ser},L_0} = 1 \text{ m}\Omega$ and $R_{\text{ser},C_0} = 0 \text{ m}\Omega$. Circuit components chosen to $C_0 = 10 \mu\text{F}$, $L_0 = 10 \mu\text{H}$ and $R_0 = 10 \Omega$, $\Delta = 0 \text{ F}$ and $C_g = 0 \text{ F}$. Implementation of defect section of size 3×4 unit cells at the *x*-boundary. Excitation at node $(16|1|B)$ shown in the figure by a green frame marking the corresponding unit cell. (b) and (c) 10×10 unit cells with *A* – *B*-termination in *x*- and *y*-direction, implementing realistic operational amplifiers (*LTSpice* model LT1363). Circuit components chosen to $C_0 = 0.1 \mu\text{F}$, $L_0 = 1 \mu\text{H}$, $R_0 = 30 \Omega$, $\Delta = 0 \text{ F}$ and $C_g = 0 \text{ F}$. Parasitic effects of the components $R_{\text{ser},L_0} = 150 \text{ m}\Omega$ and $R_{\text{ser},C_0} = 5 \text{ m}\Omega$. Excitation at node $(1|4|A)$ shown in the figure by a green frame marking the corresponding unit cell. For (c), edge INIC connections to ground are adapted to be $R_0 = 36 \Omega$ for the positive and $R_0 = -16 \Omega$ for the negative component.

packet that inherits the form of a Gaussian distribution of width $\Delta\omega_{\text{exc}}$ centered around the frequency ω_c Fourier transformed into the time domain. Due to the peaked excitation in real space, the eigenstates corresponding to all wave vectors \mathbf{k} are excited equally from the viewpoint of reciprocal distribution. Consequently, the only limitation of the excitation of eigenmodes is imposed by the distribution of $\Delta\omega_{\text{exc}}$ in frequency space. The bulk band gap value in frequency space is given by $\omega_{\text{gap}} = \frac{\sqrt{3}}{2R_0C_0}$. For an unaltered system size and

Gaussian distribution of width $\Delta\omega_{\text{exc}}$ centered around the middle of the frequency band gap ω_0 , an increase in the band gap ω_{gap} leads to a decrease in the excitation of the number of \mathbf{k} -eigenvectors as well as to a decrease in the magnitude of their excitation, because the eigenfrequencies in \mathbf{k} are more spread out in frequency space due to the larger gap value. Of course, this statement also depends on the type of edge termination, where we will have more \mathbf{k} -points along the edge band in a bearded edge compared to the zigzag edge due to the band spreading being twice as large in \mathbf{k} -space.

In Fig. 6, we show *LTS*pice simulations of three different implementations of the TCC, showing the voltage profile of the whole circuit board at different time frames. In Fig. 6a, the circuit size is chosen to 20×20 unit cells with $B - A$ termination in both x - and y -direction along with a defect section of size 3×4 unit cells at the x -boundary cut out of the circuit by grounding the corresponding nodes. The parameters of the circuit are chosen to $C_0 = 10 \mu\text{F}$, $L_0 = 10 \mu\text{H}$ and $R_0 = 10 \Omega$, $\Delta = 0 \text{ F}$ and $C_g = 0 \text{ F}$. We further employ ideal operational amplifiers in the circuit, that are simulated as ideal voltage controlled current sources. We use a current source to excite the circuit at the node $(16|1|B)$ (shown by a green framing marking the corresponding unit cell) by a Fourier transformed Gauss distribution of width $\Delta\omega_{\text{exc}} = 0.4 \text{ kHz}$ centered around the frequency $w_c = 9.2 \text{ kHz}$. The parasitic serial resistance was chosen $R_{\text{ser},L_0} = 1 \text{ m}\Omega$ for the inductors and to $R_{\text{ser},C_0} = 0 \text{ m}\Omega$ for the capacitors.

In Fig. 6b and 6c, the circuit size is chosen to 10×10 unit cells with $A - B$ termination in both x - and y -direction. The circuit parameters are $C_0 = 0.1 \mu\text{F}$, $L_0 = 1 \mu\text{H}$, $R_0 = 30 \Omega$, $\Delta = 0 \text{ F}$ and $C_g = 0 \text{ F}$. In this simulation, we use a realistic model for the operational amplifiers in the circuit (*LTS*pice LT1363). We again use a current source to excite the circuit at the node $(1|4|A)$ with a Gaussian wave packet of width $\Delta\omega_{\text{exc}} = 20 \text{ kHz}$ and central frequency $w_c = 290 \text{ kHz}$. The parasitic effects of the components are $R_{\text{ser},L_0} = 150 \text{ m}\Omega$ and $R_{\text{ser},C_0} = 5 \text{ m}\Omega$.

In Fig. 6a,b,c, we show the time-resolved propagation of the edge modes for the same system parameters used in the time integration plots in Fig. 3a,e,f in the main text. This plot proves the propagation of the edge localized mode along the boundary of the TCC in real space. Fig. 6a shows the propagation of the mode along the boundary of the TCC unhindered by the occurrent defect area, at which it is traveling around. This demonstrates the topological character of the edge mode, which prevails at any type of circuit boundary termination. By inspecting Fig. 6b and 6c, it becomes clear, that the decay length of the mode in 6b, where realistic parasitic effects of $R_{\text{ser},L} = 150 \text{ m}\Omega$ and $R_{\text{ser},C} = 5 \text{ m}\Omega$ are taken into account is much smaller than for the mode in 6c, where the same parasitics are used, but slightly corrected for by adapting the edge INIC connections to ground $R_{0,+} = 36 \Omega$ for the positive and $R_{0,-} = -16 \Omega$ for the negative component instead of $R_{0,+} = 30 \Omega$ and $R_{0,-} = -30 \Omega$. The correction was calculated by assuming the resistive component in the inductor only and computing the real part of the admittance of the series connection of inductance and resistance to

$$\Re (Z_{\text{L,para}}) = \frac{R_{\text{ser},L}}{R_{\text{ser},L}^2 + (\omega L)^2}. \quad (39)$$

We correct this real part, occurring at the level of the unit matrix in the Laplacian, by raising the absolute value of the conductance for the effective negative resistances and analogously lowering the conductance for the positive resistances, which both arise due to the INIC connections to ground.